Supporting Information: Probing Exfoliated Graphene Layers and Their Lithiation with Micro-Focused X-Rays

Patrik Zielinski,[†] Matthias Kühne,[†,¶] Daniel Kärcher,[†] Federico Paolucci,[†,§] Peter Wochner,[†] Sven Fecher,[†] Jakub Drnec,[‡] Roberto Felici,[‡] and Jurgen H. Smet[*,†]

[†]*Max Planck Institute for Solid State Research, 70569 Stuttgart, Germany*

[‡]*European Synchrotron Radiation Facility (ESRF), 38000 Grenoble, France*

[¶]*Current address: Department of Chemical Engineering, Massachusetts Institute of Technology, Cambridge, Massachusetts 02139, USA*

[§]*Current address: INFN Sezione di Pisa, 56127 Pisa, Italy*

E-mail: j.smet@fkf.mpg.de

Modeling specular X-ray reflectivity (XRR)

The intensity of X-rays reflected from a surface is determined by the (complex) index of refraction n. In the X-ray region of the electromagnetic spectrum it can be written as

$$n = 1 - \delta - i\beta, \tag{1}$$

Table S1: Forward atomic scattering factors at two different X-ray beam energies. From http://henke.lbl.gov/optical_constants/asf.html, last accessed on 29 Jan 2019.

	Si		O		C	
	$f_{1,\mathrm{Si}}(0)$	$f_{2,\mathrm{Si}}(0)$	$f_{1,\mathrm{O}}(0)$	$f_{2,\mathrm{O}}(0)$	$f_{1,\mathrm{C}}(0)$	$f_{2,\mathrm{C}}(0)$
12.0 keV ($\lambda = 1.033$ Å)	14.150	0.149	8.025	$1.41 \cdot 10^{-2}$	6.009	$3.87 \cdot 10^{-3}$
18.5 keV ($\lambda = 0.670$ Å)	14.074	0.062	8.010	$0.53 \cdot 10^{-2}$	6.003	$1.40 \cdot 10^{-3}$

where δ and β describe the dispersive and absorptive behavior, respectively. δ and β depend on the X-ray wavelength λ and may be stated as[S1]

$$\delta = \frac{r_e \lambda^2}{2\pi} \sum_j^J \nu_j f_{1,j}(0), \tag{2}$$

$$\beta = \frac{r_e \lambda^2}{2\pi} \sum_j^J \nu_j f_{2,j}(0). \tag{3}$$

Here, $r_e = 2.8179$ fm is the classical electron radius and ν_j is the number of atoms of type j (per unit volume) in a material consisting of J different atomic species. $f_j(0) = f_{1,j}(0) + i f_{2,j}(0)$ is the tabulated forward atomic scattering factor of species j at wavelength λ. For the relevant X-ray beam energies of 12 keV ($\lambda = 1.033$ Å) and 18.5 keV ($\lambda = 0.670$ Å), $f_{2,j}(0)$ is tiny and $f_{1,j}(0) \approx Z$ for the elements (with atomic number Z) constituting our samples (see Tab. S1). δ is related to the critical angle of total reflection $\theta_\mathrm{c} = \sqrt{2\delta}$. One may further define the number density of a material as

$$\nu_a = \frac{\rho \cdot N_A}{M}, \tag{4}$$

where ρ is its mass density, M is its molar mass, and N_A is the Avogadro constant. $\nu_a = \nu_j$ only holds for non-molecular elemental materials, with $j = J = 1$ and $M = A_r$ g/mol (A_r is the dimensionless relative atomic mass). For compounds such as SiO_2 with $J = 2$ and $M = 60.08$ g/mol, the number of atoms per unit volume are $\nu_1 = \nu_a$ for Si and $\nu_2 = 2 \cdot \nu_a$ for O.

The intensity I of specularly reflected X-rays of wavelength λ, incident onto the surface

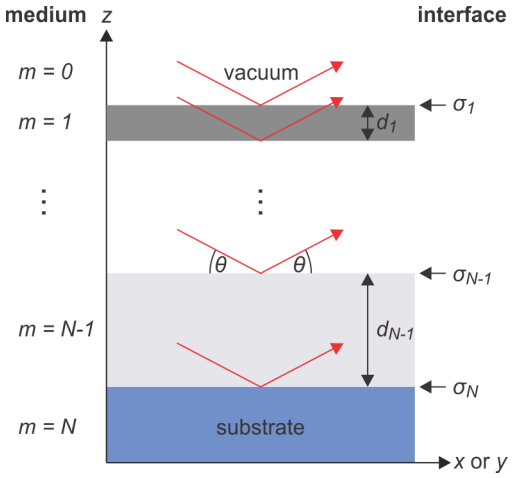

Figure S1: Schematic multilayer representation of a flat sample probed by specular X-ray reflectivity as described within Parratt's recursion formalism. Red arrows represent X-rays incident onto the sample at an angle θ with respect to the surface.

of a flat sample under an angle θ, is determined by the sample's composition at and near its surface (within a certain depth z into the bulk). To calculate this intensity, Parratt[S2] introduced a recursive formalism approximating a flat sample as a slab consisting of N superposed layers (of different, homogeneous composition) oriented parallel to the probed surface, see Fig. S1 for a schematic. The refractive index of each layer m is $n_m = 1-\delta_m-i\beta_m$, and the critical angle of total reflection is $\theta_{c,m} = \sqrt{2\delta_m}$. Each layer m is characterized by its thickness d_m and its mass density ρ_m. Allowing for finite roughness s_m at interfaces between layers,[S3] the recursion formula can be written as

$$r_{m-1} = a_{m-1}^4 \frac{\frac{f_{m-1}-f_m}{f_{m-1}+f_m} s_m + r_m}{1 + r_m \frac{f_{m-1}-f_m}{f_{m-1}+f_m} s_m}, \tag{5}$$

where

$$a_m = \exp\left(-i\frac{\pi}{\lambda} f_m d_m\right), \tag{6}$$

$$f_m = \sqrt{\sin(\theta)^2 - (\theta_{c,m})^2 - 2i\beta_m}, \tag{7}$$

and

$$s_m = \exp\left[-2\left(\frac{2\pi}{\lambda}\right)^2 \sigma_m^2 f_m f_{m-1}\right]. \tag{8}$$

Here, a_m is an amplitude factor and f_m is a Fresnel reflection coefficient. σ_m denotes the root mean square (rms) density variation at the interface between layers m and $m-1$ (see

Fig. S1). XRR cannot distinguish between a rough interface at $z = z_m$ between two media with refractive indices n_m and n_{m-1} and a profile of the refractive index $n_m(z)$ that varies smoothly across the interface. As long as the thicknesses d_m and d_{m-1} exceed σ_m, the Névot-Croce factor s_m may thus be derived using[S4]

$$n_m(z) = \frac{n_m + n_{m-1}}{2} - \frac{n_m - n_{m-1}}{2}\mathrm{erf}\left(\frac{z - z_m}{\sqrt{2}\sigma_m}\right). \tag{9}$$

For a given angle θ, Eq. 5 is calculated in recursive manner starting with $m = N$ and ending with $m = 1$. Since the sample is penetrated only little by X-rays in the relevant case of small θ, the substrate may be considered infinitely thick and hence $r_N = 0$. The intensity of X-rays specularly reflected from the sample is obtained as

$$I(\theta) = I_0|r_0|^2, \tag{10}$$

where I_0 is the intensity of the incident X-ray beam.

Due to the finite lateral extent of both the graphene flake and its supporting Si substrate, depending on θ the footprint of the incident X-ray beam may exceed either the former or even both (see Figs. 3a-c and S2a-c). We approximate the profile of the incident X-ray beam by an ellipse of width $2w$ and height $2h$ (w and h are the semi axes parallel to y and $z \cdot \cos\theta$, respectively) as shown in Fig. S2d. The width of the footprint on the sample is identical to $2w$ irrespective of θ. This is not the case for its length $2h'$. Instead, $h' = h/\sin\theta$. The area of the elliptical X-ray beam footprint is thus

$$A_{\mathrm{bfp}} = \pi w h'(\theta) = \pi w \frac{h}{\sin\theta}. \tag{11}$$

A_{bfp} has to be compared to both the lateral dimensions of a given graphene flake under study as well as of its supporting substrate. Especially at low angles θ, the X-ray beam footprint falls only partially on the graphene flake (probed area A_{G}). Another part of area $A_{\mathrm{SiO_2}}$

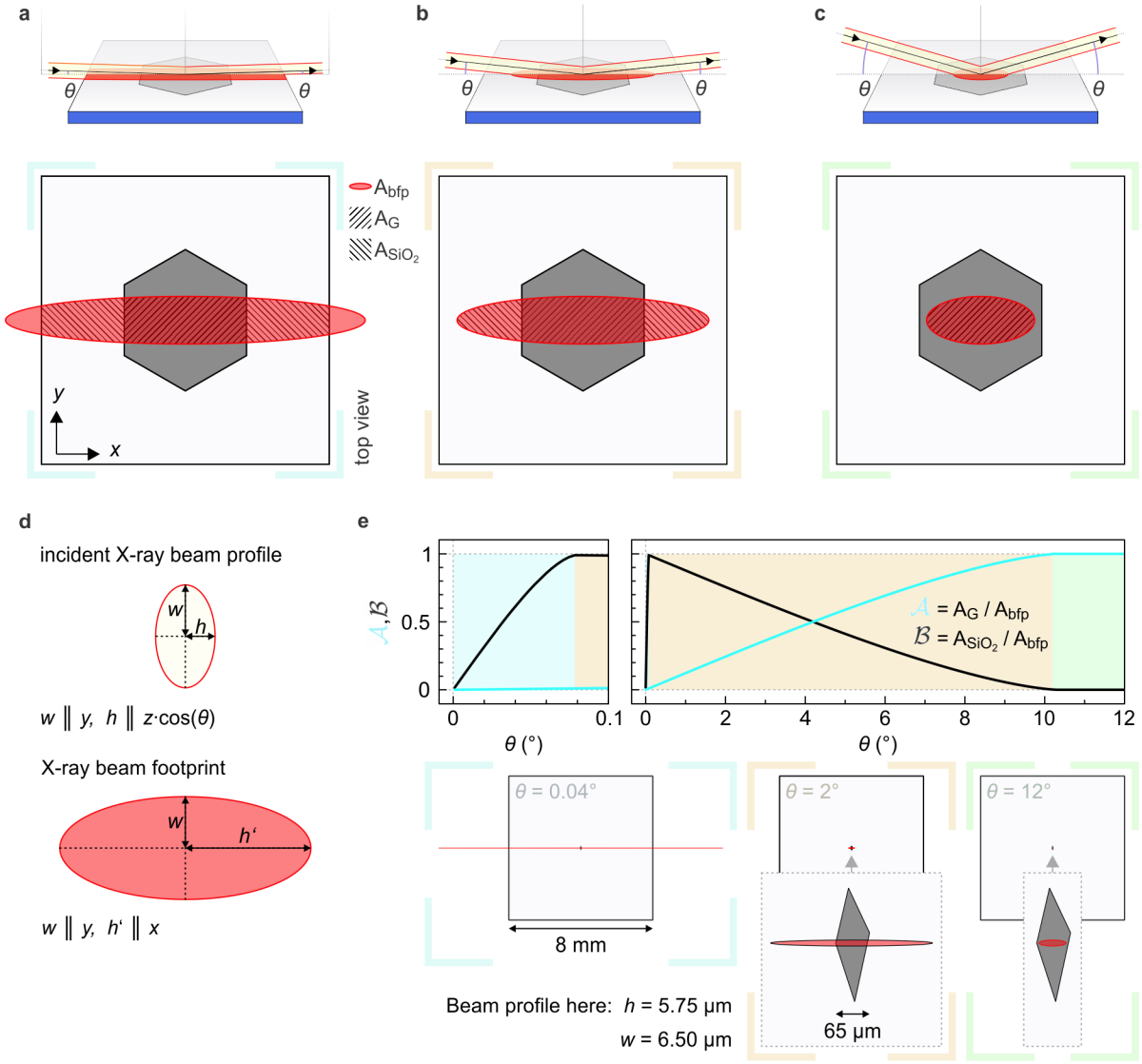

Figure S2: Schematic of the X-ray beam footprint (red ellipse) on a sample consisting of a graphene flake (dark grey) supported on a SiO_2-terminated Si substrate (light grey), similar to Figs. 3a-c in the main text. (a-c) Illustration of the repartition of the X-ray beam footprint area for increasing incidence angle θ. Schematic top views are included in the bottom row. (d) Elliptical profiles of the incident X-ray beam (upper part) and of its footprint on the sample (lower part). (e) Exemplary θ-dependence of the weighting factors $\mathcal{A}$ and $\mathcal{B}$ required for Eq. 12. The lower row shows snapshots of the substrate, graphene flake and footprint areas at three different values θ from which the weighting factors were computed. This example corresponds to the case of the bilayer graphene sample of Fig. 3d in the main text.

falls on the graphene-uncovered substrate, see Figs. S2a-c. Taking into account the lateral dimensions of both a given graphene flake and its SiO_2-terminated Si substrate, $A_G(\theta)$ and $A_{SiO_2}(\theta)$ are determined in straight forward manner by geometrical computation (Boolean

operations on surfaces). Consequently, the intensity of specularly reflected X-rays (Eq. 10) comprises two weighted contributions and may be rewritten as

$$I(\theta) = I_0 \cdot |\mathcal{A} \cdot r_{0,\mathrm{G}} + \mathcal{B} \cdot r_{0,\mathrm{SiO_2}}|^2, \tag{12}$$

where $r_{0,\mathrm{G}}$ and $r_{0,\mathrm{SiO_2}}$ are the computed recursions (Eq. 5) for the graphene flake-covered and -uncovered parts of the sample, respectively. The weighting factors are

$$\mathcal{A} = \frac{A_\mathrm{G}}{A_\mathrm{bfp}} \qquad\qquad \mathcal{B} = \frac{A_\mathrm{SiO_2}}{A_\mathrm{bfp}} = 1 - \frac{A_\mathrm{G}}{A_\mathrm{bfp}}. \tag{13}$$

In the upper panel of Fig. S2e, we plot $\mathcal{A}(\theta)$ and $\mathcal{B}(\theta)$ for the case of the graphene bilayer shown in Fig. 3d (main text). As is to be expected, $\mathcal{B}$ dominates at small θ and $\mathcal{A}$ dominates at larger θ. The initial steep increase of $\mathcal{B}(\theta)$ up to $\theta_\mathrm{S} = 0.08°$ reflects the finite lateral extent of the substrate $l_\mathrm{SiO_2} = 8\,\mathrm{mm}$, as $\theta_\mathrm{S} = \arcsin(2h/l_\mathrm{SiO_2}) = 0.08°$. This causes the well-known $\frac{\sin\theta}{\sin\theta_\mathrm{S}}$-type increase in reflected intensity in the total-external-reflection regime.[S4,S5]

The XRR of a multi-layered sample is determined by the profile of electron density perpendicular to the sample surface, i.e., in z-direction. Fig. 3d in the main text shows two schematic examples in its side panels. Here, to first approximation, the densities ρ_Si of the Si substrate and $\rho_\mathrm{SiO_2}$ of the SiO_2 layer are both assumed independent of z. We model a multi-layered graphene flake assuming identical Gaussian density profiles for each atomic layer. The resulting effective mass density profile[S4] of a flake consisting of k graphene sheets stacked upon each other such that neighboring sheets are separated by a distance c can then be described as

$$\rho_\mathrm{g}(z) = R \cdot \sum_{u=1}^{k} \exp\left[-\frac{(z - u \cdot c)^2}{2q^2}\right]. \tag{14}$$

Here, q is related to the full width at half maximum (FWHM) of each Gaussian as FWHM =

$2q\sqrt{2\ln 2}$ and R is determined by requiring

$$\int_{-\infty}^{\infty} \rho_{\mathrm{g}}(z)\,\mathrm{d}z = k \cdot \rho_{\mathrm{G}} \cdot c_{\mathrm{G}}, \tag{15}$$

where the bulk density of graphite ρ_{G} times the interlayer spacing in graphite $c_{\mathrm{G}} = 0.335\,\mathrm{nm}$ yields the areal density of one graphene sheet. We thus find $R = \rho_{\mathrm{G}} c_{\mathrm{G}}/q\sqrt{2\pi}$. In order to use Eq. (14) in Eq. (5), we discretize $\rho_{\mathrm{g}}(z)$ into slices of equal width Δz as schematically shown in Fig. S3. The density $\rho_g(m \cdot \Delta z)$ of each slice m is a constant. Here, m is the same index as in Eqs. (1)-(4). Note that $m = N$, $m = N-1$, and $m = 0$ denote the Si-substrate, the SiO_2-layer, and the surrounding atmosphere (vacuum), respectively. Therefore, $m = N-2, \ldots, 1$ is the index range for the slices of $\rho_{\mathrm{g}}(z)$. Since Gaussian distributions are defined everywhere in z but N is finite, we choose the $m = 1$ slice such that 95 % of the integrated area of the kth Gaussian (the uppermost in z) are taken into account, equivalent to approximately two standard deviations.

Graphene is known to partially conform to the underlying SiO_2 (see Fig. S4a).[S6,S7] We account for this in our calculations as follows. We calculate the θ-dependent XRR response for a density profile representing our systems as described above, however, with a flat SiO_2 surface (zero roughness). We repeat this calculation for different SiO_2 thicknesses $d'_{\mathrm{SiO_2}}$. Then we average all calculated XRR curves in weighted fashion. The probability $p(d'_{\mathrm{SiO_2}})$ for each calculated curve to contribute to the overall XRR response decreases the more $d'_{\mathrm{SiO_2}}$ deviates from the real value $d_{\mathrm{SiO_2}}$. $p(d'_{\mathrm{SiO_2}})$ is determined by integrating the probability distribution function (PDF), a normalized Gaussian centered at $d_{\mathrm{SiO_2}}$ with standard deviation $\sigma_{\mathrm{SiO_2}}$ (to reproduce the Névot-Croce result for the SiO_2 surface, Eq. 8), within $\pm\Delta z/2$ around $d'_{\mathrm{SiO_2}}$ (see Fig. S4b). Here, Δz is the interval in $d'_{\mathrm{SiO_2}}$ for which calculations are performed. In the Névot-Croce approach, the distance b of graphene from the SiO_2 surface (centered at $d_{\mathrm{SiO_2}}$) is fixed. In contrast, our approach allows to keep b locked to each $d'_{\mathrm{SiO_2}}$, thereby mimicking conformal adhesion. We find the overall XRR response thus calculated to typically reveal

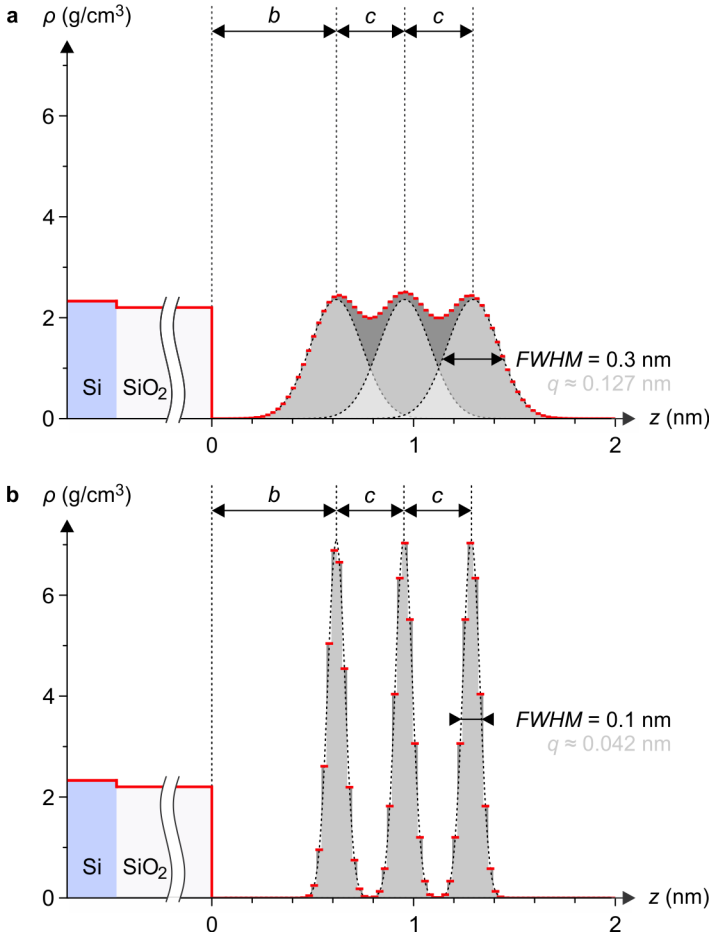

Figure S3: Schematic density profiles for a 3-layer graphene flake supported on a SiO_2-terminated Si substrate. The z-dependent density of graphene sheets is approximated by Gaussian distributions according to Eq. (14). For illustration purposes, we show two extreme scenarios with (a) $q \approx 0.127\,\text{nm}$ and (b) $q \approx 0.042\,\text{nm}$.

signatures of the graphene system to an extent that agrees better with the experiment. Fig. S4c is an example, where the orange (blue) curve is calculated for identical parameters but without (with) conformation.

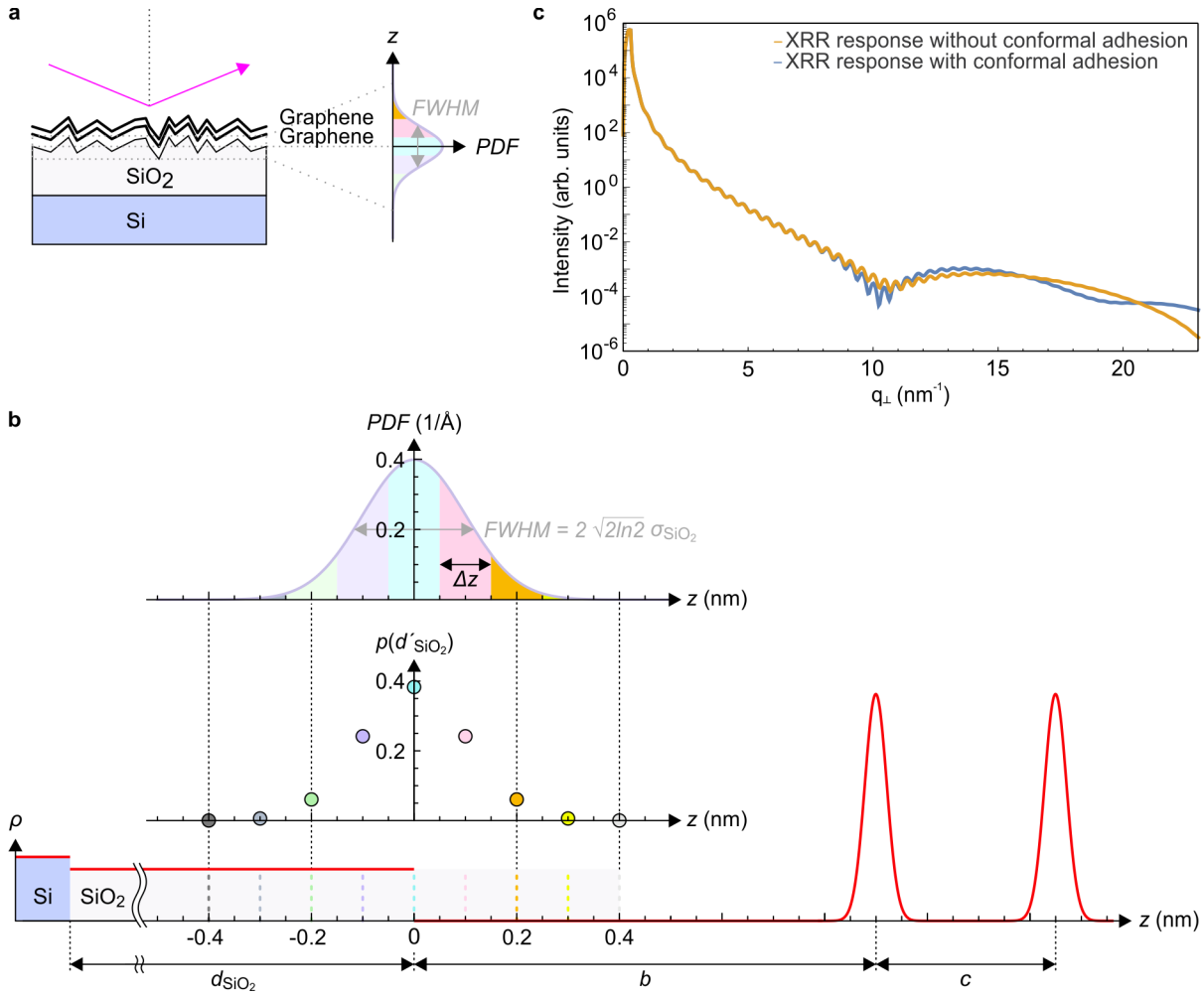

Figure S4: (a) Schematic of conformation of graphene to the roughness of the underlying SiO_2. (b) Schematic illustrating how the normalized Gaussian-shaped PDF characterized by the standard deviation σ_{SiO_2} relates to $p(d'_{SiO_2})$, the weight of the contribution of the calculated XRR response of a system with d'_{SiO_2} to the overall XRR response. (c) Exemplary calculations of the overall XRR response of a bilayer graphene system on SiO_2, without (orange) and with (blue) conformal adhesion taken into account as described in the text.

In Figs. S5–S7 we again show the measured and calculated data as in Figs. 3–5, respectively. In the lower panel of those figures, we plot the difference between the curves shown in each corresponding upper panel. This emphasizes the contribution of bilayer graphene to the overall XRR response in Fig. S5a, featuring a characteristic minimum at intermediate values of $q_\perp$. In panels b and c of this figure, we compare each measured dataset with the calculated XRR response for which best agreement was obtained. The difference curves reveal finite, yet small variations around zero. Lithiation shifts the graphene bilayer-related minimum in the experimental XRR response to lower values in $q_\perp$ (see Fig. S6a). This becomes similarly apparent for the measured 10 layer graphene flake in Fig. S7a where the position of all extrema appears downshifted in $q_\perp$. Again in panels b and c, we compare our experimental data to calculations for which best agreement was obtained. The extent to which calculations reproduced positions of XRR extrema served as guiding principle for determining a good match to the data.

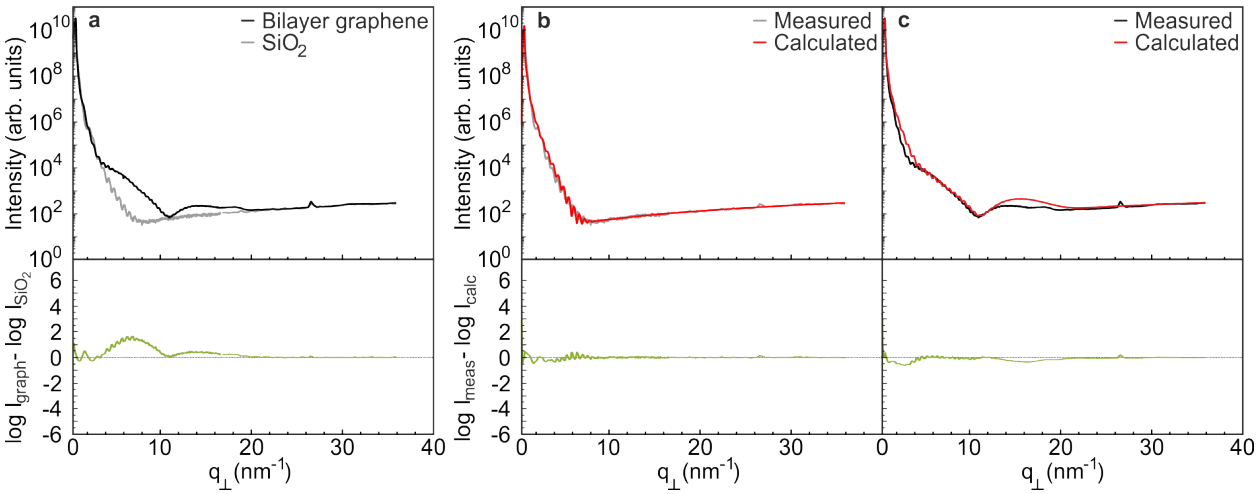

Figure S5: Measured and calculated XRR data as in Fig. 3e. (a) Measured XRR of bilayer graphene as well as of the bare SiO_2-terminated Si substrate as. (b) Measured and calculated XRR response of the substrate. (c) Measured and calculated XRR response of bilayer graphene. Each lower panel shows the difference between curves plotted in the corresponding upper panel.

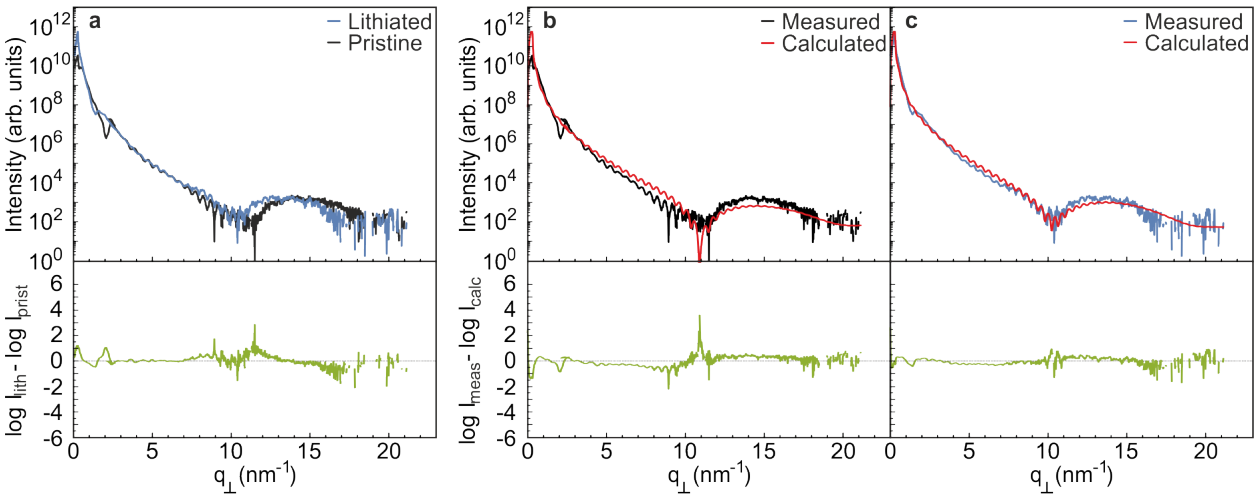

Figure S6: Measured and calculated XRR data of the bilayer graphene flake in Fig. 4a. (a) XRR response measured before and during lithiation. (b) Measured and calculated XRR response of the pristine flake. (c) Measured and calculated XRR response of the lithiated flake. Each lower panel shows the difference between curves plotted in the corresponding upper panel.

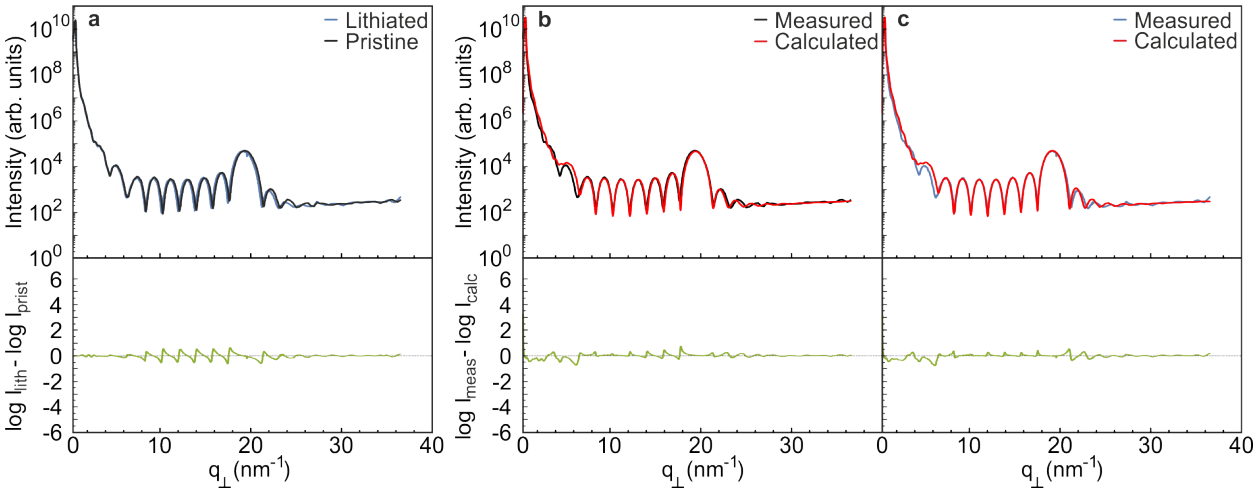

Figure S7: Measured and calculated XRR data of the 10 layer graphene flake in Fig. 5a. (a) XRR response measured before and during lithiation. (b) Measured and calculated XRR response of the pristine flake. (c) Measured and calculated XRR response of the lithiated flake. Each lower panel shows the difference between curves plotted in the corresponding upper panel.

Beam-induced contamination

With the polymer electrolyte present, we systematically observe beam-induced contamination on the sample surface after having performed XRR measurements. In scanning electron micrographs, this contamination appears as broad, dark streaks located where the synchrotron beam irradiated the sample. Three such micrographs are displayed in the top row of Fig. S8. Using atomic force microscopy, we extract height profiles of the contamination at two different locations for each sample (lower row). The thickness tends to be larger at areas that received more integrated irradiation. The deposited material is possibly due to hydrocarbons cracked by X-ray photons or photoelectrons.[S8–S10] Among different possible sources, hydrocarbons likely originate from our solidified polymer electrolyte that contains species with non-negligible vapor pressure.

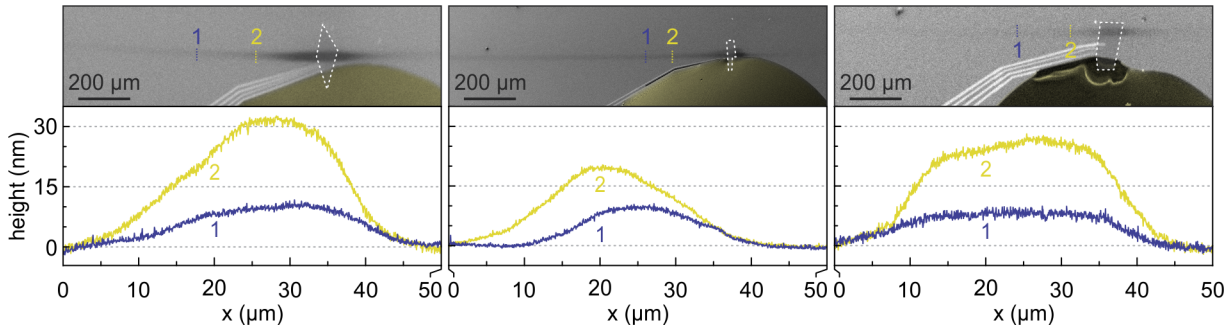

Figure S8: Scannning electron micrographs of three samples acquired after XRR measurements (top row). The rim of each graphene flake is demarcated by a white dashed line. The polymer electrolyte is colored yellow. A near-horizontal broad, dark streak easily visible in each micrograph is due to beam-induced contamination. Lower row shows height profiles (obtained by atomic force microscopy) across the beam-induced contamination at two locations indicated in the respective top panel.

References

(S1) Henke, B.; Gullikson, E.; Davis, J. X-Ray Interactions: Photoabsorption, Scattering, Transmission, and Reflection at $E = 50 - 30,000\,\mathrm{eV}$, $Z = 1 - 92$. *At. Data Nucl. Data Tables* **1993**, *54*, 181–342.

(S2) Parratt, L. G. Surface Studies of Solids by Total Reflection of X-Rays. *Phys. Rev.* **1954**, *95*, 359–369.

(S3) Névot, L.; Croce, P. *Rev. Phys. Appl. (Paris)* **1980**, *15*, 761–779.

(S4) Tolan, M. *X-Ray Scattering from Soft-Matter Thin Films*; Springer Tracts in Modern Physics; Springer-Verlag Berlin Heidelberg, 1999; Vol. 148.

(S5) Gibaud, A.; Vignaud, G.; Sinha, S. K. The correction of geometrical factors in the analysis of X-ray reflectivity. *Acta Crystallogr. A* **1993**, *49*, 642–648.

(S6) Ishigami, M.; Chen, J. H.; Cullen, W. G.; Fuhrer, M. S.; Williams, E. D. Atomic Structure of Graphene on SiO_2. *Nano Lett.* **2007**, *7*, 1643–1648.

(S7) Cullen, W. G.; Yamamoto, M.; Burson, K. M.; Chen, J. H.; Jang, C.; Li, L.; Fuhrer, M. S.; Williams, E. D. High-Fidelity Conformation of Graphene to SiO_2 Topographic Features. *Phys. Rev. Lett.* **2010**, *105*, 215504.

(S8) Boller, K.; Haelbich, R.-P.; Hogrefe, H.; Jark, W.; Kunz, C. Investigation of carbon contamination of mirror surfaces exposed to synchrotron radiation. *Nucl. Instr. Meth. Phys. Res.* **1983**, *208*, 273–279.

(S9) Rosenberg, R. A.; Mancini, D. C. Deposition of carbon on gold using synchrotron radiation. *Nucl. Instr. Meth. Phys. Res. A* **1990**, *291*, 101–106.

(S10) Kurt, R.; van Beek, M.; Crombeen, C.; Zalm, P.; Tamminga, Y. In *Emerging Lithographic Technologies VI*; Engelstad, R. L., Ed.; Proc. of SPIE; 2002; Vol. 4688; pp 702–709.